Large grain growth for hole-conductor-free fully printable perovskite solar cells via polyoxometalate molecular doping

Yuzhuo Zhang, Yanju Wang, Zhixia Sun, Fengyan Li,* Ran Tao, Zhanbin Jin, and Lin Xu*

Key Laboratory of Polyoxometalate Science of Ministry of Education, Department of Chemistry, Northeast Normal University, Changchun, Jilin 130024, P. R. China.

Experimental Section

S1. Materials and Synthesis

CH_3NH_3I (MAI) and $HOOC(CH_2)_4NH_3I$ (5-AVAI) were synthesized according to reported procedure:[1] Hydroiodic acid (Sinopharm) together with methylamine (Amethyst) or 5-aminopentanoic acid (Sigma) were added with a mole ratio of 1:1 into round-bottom flask and stirred in the ice bath for 2h. After stirring at 0°C for 2h, the resulting solution was evaporated at 50°C until the solvent completed evaporated and the raw product synthesized. The precipitate was washed three times with diethyl ether and dried at 60°C under vacuum and used without further purification. The $(5\text{-}AVA)_x(MA)_{1-x}PbI_3$ precursor solution was prepared according to literature method.[1] PW_{12} was prepared according to literature method.[2] The $(5\text{-}AVA)_x(MA)_{1-x}PbI_3/PW_{12}$ precursor was prepared by adding PW_{12} into $(5\text{-}AVA)_x(MA)_{1-x}PbI_3$ precursor under continuous stirring until the PW_{12} was completely dissolved.

S2. Fabrication of perovskite solar cell device

The hole-conductor-free fully printable mesoscopic solar cell based on a carbon CE is shown in Figure 1a. All of the films in the mesoscopic solar cell were fabricated by the reported method with a little modification.[1] Fluorine-doped tin oxide (FTO) glass was patterned by chemical etching (Zn powder and 2 M HCl) with the bridging-gap

width of roughly 1mm. Then, the etched substrate was cleaned with surfactant and rinsed with acetone and ethanol and deionized water and finally dried by air flow. A compact layer of TiO_2 was deposited by spin-coating (2000 rpm/min) from a precursor solution to act as a hole-blocking layer.[3] The mesoscopic TiO_2 layer was deposited by screen-printing of a TiO_2 slurry (P25 Degussa) and then sintered at 450 °C for 30min.[4] A 1-2μm ZrO_2 space layer was printed on the top of the TiO_2 layer using a ZrO_2 slurry, which acts as an insulating layer to prevent electrons from reaching the back contact. Finally, a carbon black/graphite counter electrode with the thickness of about 10μm was coated on the top of ZrO_2 layer by printing carbon/graphite composite slurry and consequently heating at 400 °C for 30min. After that, the resulting films were infiltrated with a 40wt% perovskite precursor solution by dropping on the top of the carbon counter electrode. The ultimate mesoscopic solar cells containing perovskite were obtained after drying at 50 °C for two hours. All these procedures were carried out on naturally ambient air and room temperature.

Characterization

Infrared spectra (IR) were recorded with a Nicolet Magna 560 FT-IR Spectrometer. X-ray diffraction (XRD) analyses were performed with a Rigaku D/max-3c X-ray diffractometer, using CuKa1 radiation (λ=1.5405A˚). Field-emission scanning electron microscopy (Hitachi SU-8010 FE-SEM) was used to investigate the surface and cross-section morphology. The photocurrent–voltage (J–V) characteristics of the solar cells with an active area of 0.07 cm^2 were measured using a Keithley 2400 Source Meter under illumination of a simulated sunlight (AM1.5, 100mW/cm^2). The External quantum efficiency (EQE) spectra were measured by a Model QE/IPCE system (PV Measurements, Inc.) in the 350-800nm wavelength range. Electrochemical impedance spectroscopy (EIS) was performed on a CHI660C electrochemical workstation (Shanghai, China). The fluorescence spectra were

recorded on the FL900/FS920 steady-state fluorescence spectrometer. The UV−vis diffuse reflectance spectroscopy (DRS) was recorded with a UV-Vis-NIR Spectrophotometer (Varian).

Figures and Comments

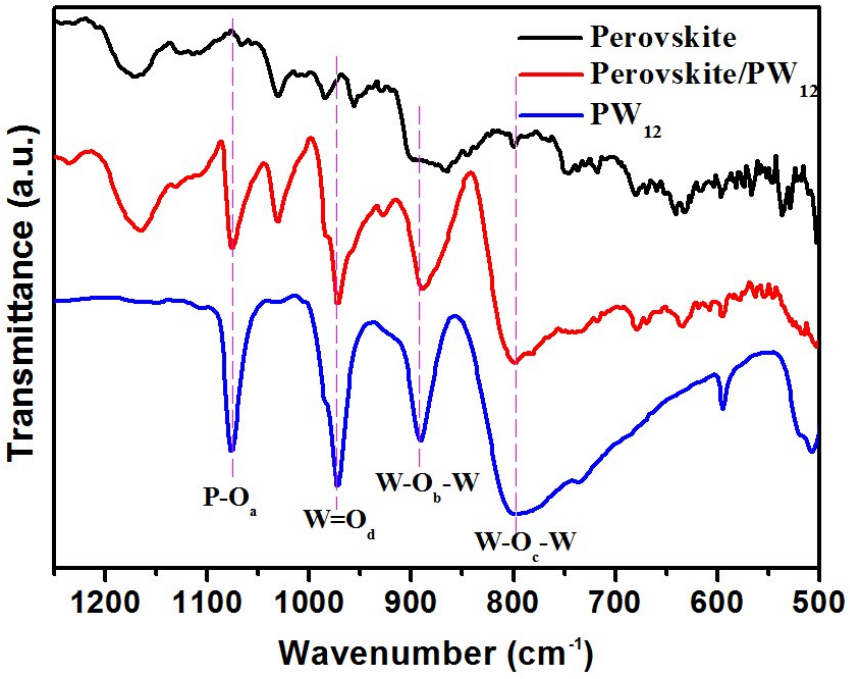

Figure S1. IR spectra. Dash lines denote characteristic peaks of POMs.

Figure S1 displayed the IR spectra of the pure $(5\text{-AVA})_x(MA)_{1-x}PbI_3$ and the $(5\text{-AVA})_x(MA)_{1-x}PbI_3/PW_{12}$ composite. In comparison with the $(5\text{-AVA})_x(MA)_{1-x}PbI_3$ curve, the $(5\text{-AVA})_x(MA)_{1-x}PbI_3/PW_{12}$ curve exhibits characteristic bands for the PW_{12} at 700-1100 cm^{-1}. The characteristic peaks observed at 1080, 983, 890, and 798 cm^{-1} were assigned to υ_{as}(P-O), υ_{as}(W=O) and υ_{as}(W-O-W), respectively, suggesting that the Keggin structure of the PW_{12} was retained in the composite.

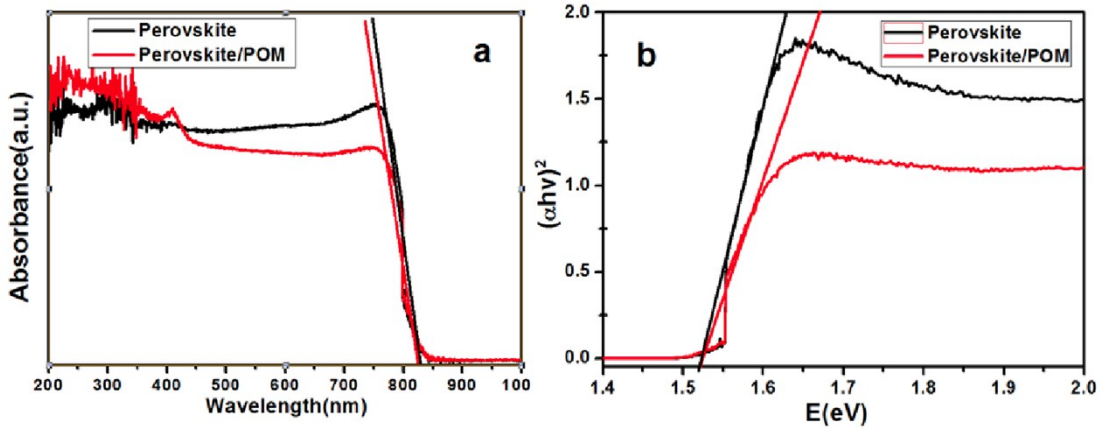

Figure S2. UV-vis diffuse reflectance spectra (a) and $(\alpha h\nu)^2$ versus light energy curves (b) of the perovskite with and without POM

As displayed in Figure S2(a), the UV-vis absorbance spectra of both the pure $(5\text{-AVA})_x(MA)_{1-x}PbI_3$ and $(5\text{-AVA})_x(MA)_{1-x}PbI_3/PW_{12}$ exhibited high light-harvesting capabilities in the spectral range from the ultraviolet to visible light. The absorption onsets of the both samples were ca. 830nm. Besides, both the curves show clear band edge cutoffs, indicating high-quality crystals with low defect concentration. Furthermore, The bandgap value was obtained on the basis of the Tauc plot as the intercept value of the plot of $(\alpha h\nu)^2$ against light energy (E). By fitting the linear region of the $(\alpha h\nu)^2$ to the energy-axis ($h\nu$) intercept as shown in Figure S2(b), The band gap (E_g) is obtained. Since PW_{12} is highly transparent in most spectral ranges, the incorporation of PW_{12} did not affect the light adsorption of $(5\text{-AVA})_x(MA)_{1-x}PbI_3$. Thus, the E_g of PW_{12} doped perovskite remain the same as the pristine perovskite (ca. 1.53eV).

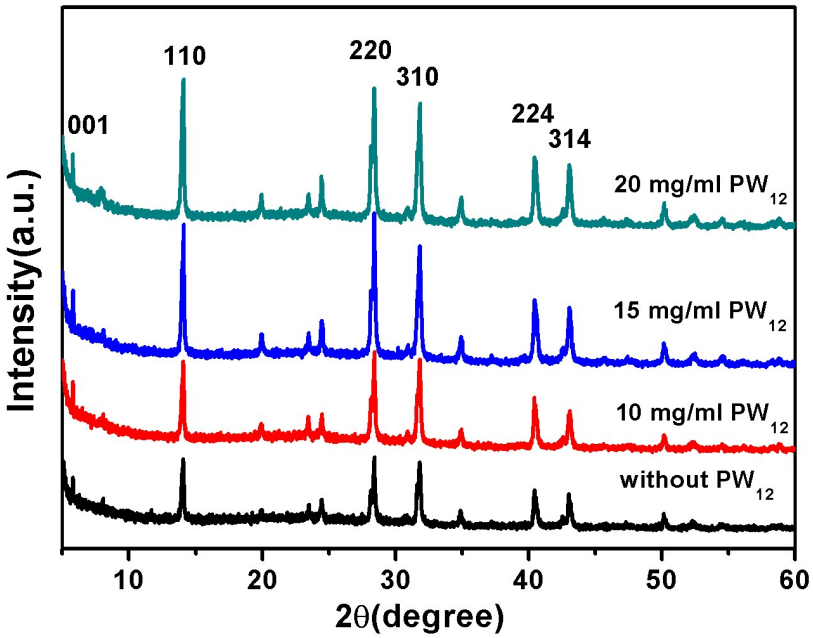

Figure S3. XRD patterns of the perovskite from 1ml precursor with 0mg, 10mg, 15mg and 20mg PW_{12} additive.

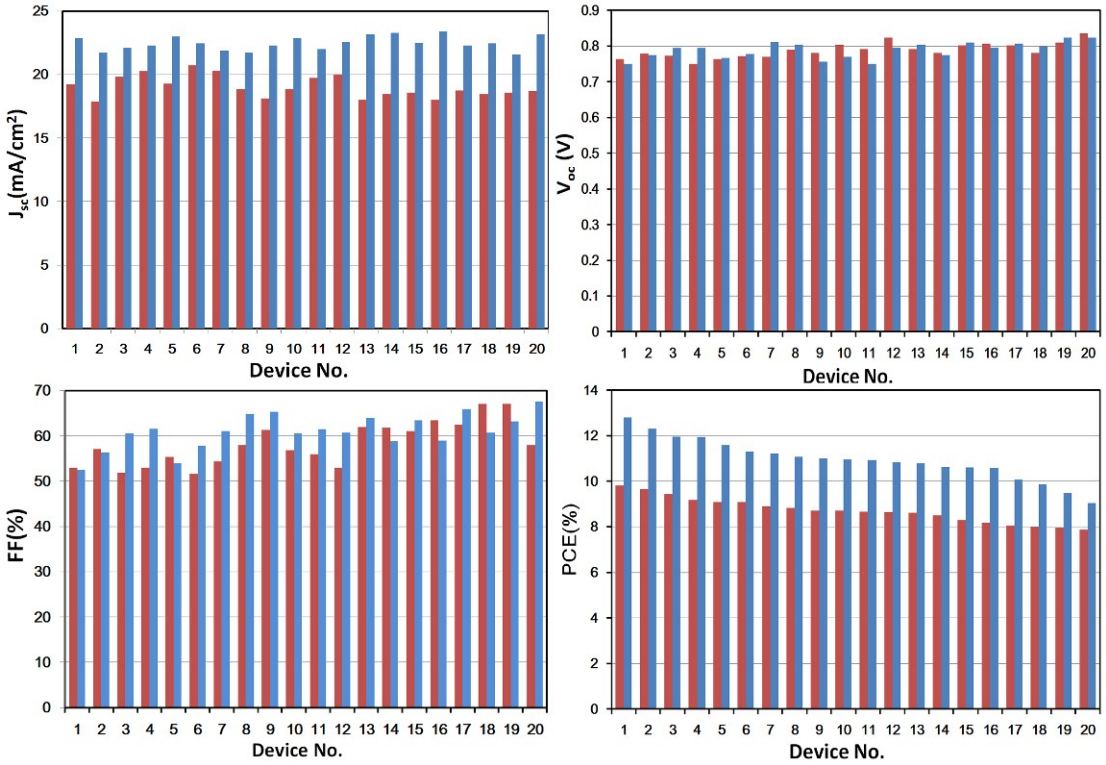

Figure S4. Statistics of photovoltaic characteristics of devices using 20 pristine (5-AVA)$_x$(MA)$_{1-x}$PbI$_3$ based devices (red) and 20 PW$_{12}$ additive devices (blue, 15mg/ml).

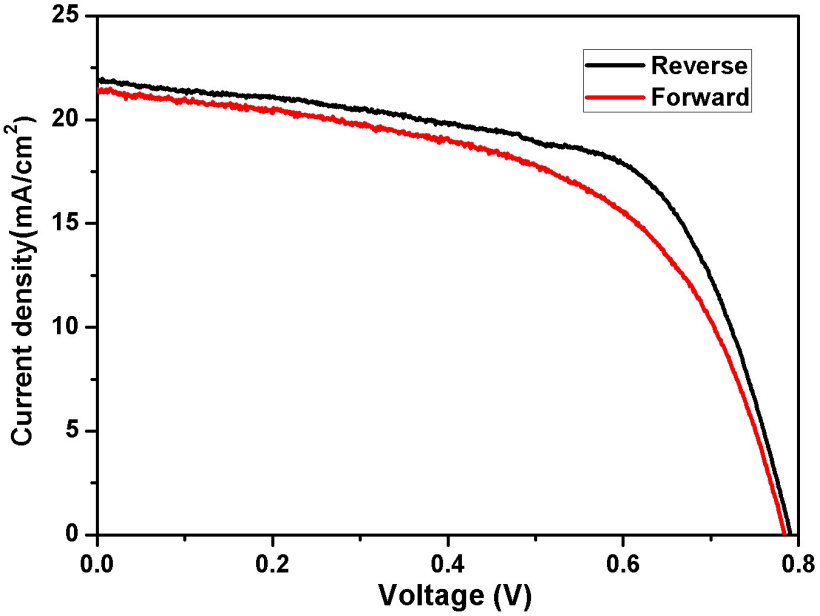

Figure S5. J-V curves of PSCs with PW$_{12}$ at different scanning directions: forward bias scan from 0V to V$_{oc}$ and back to 0V. The scanning rate was 10 mV/s.

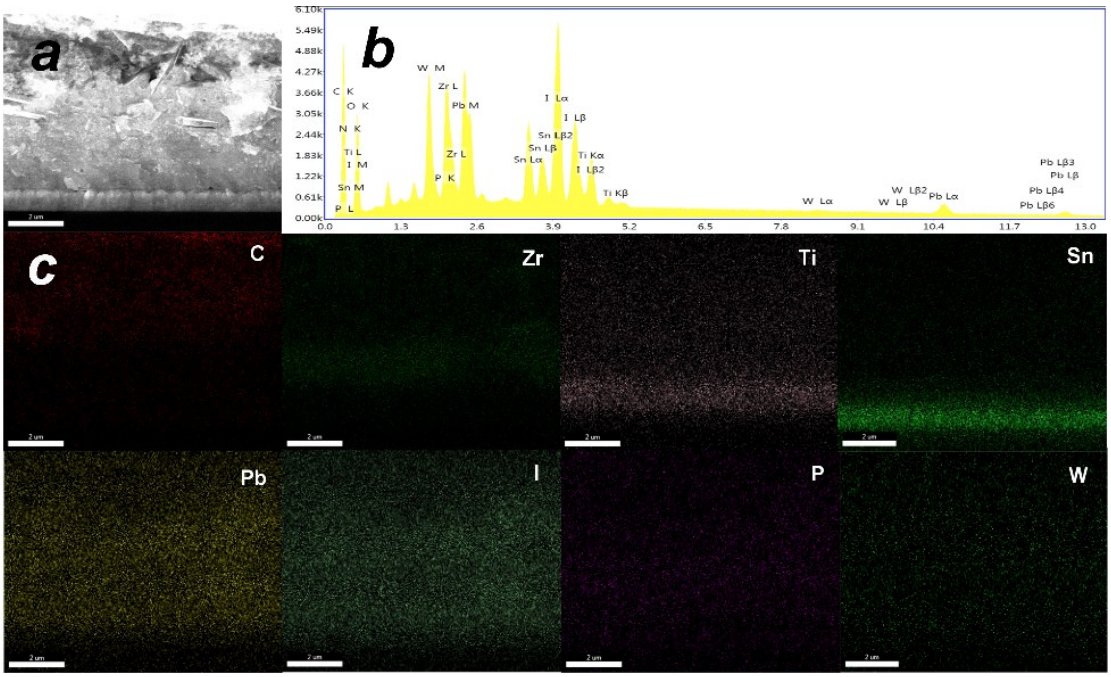

Figure S6. SEM from the cross section of the PSC device (a) with the EDX diagram (b), and the corresponding EDX elemental mappings (C, Zr, Ti, Sn, Pb, I, P and W). Note the white scale bar correspond to 2µm.

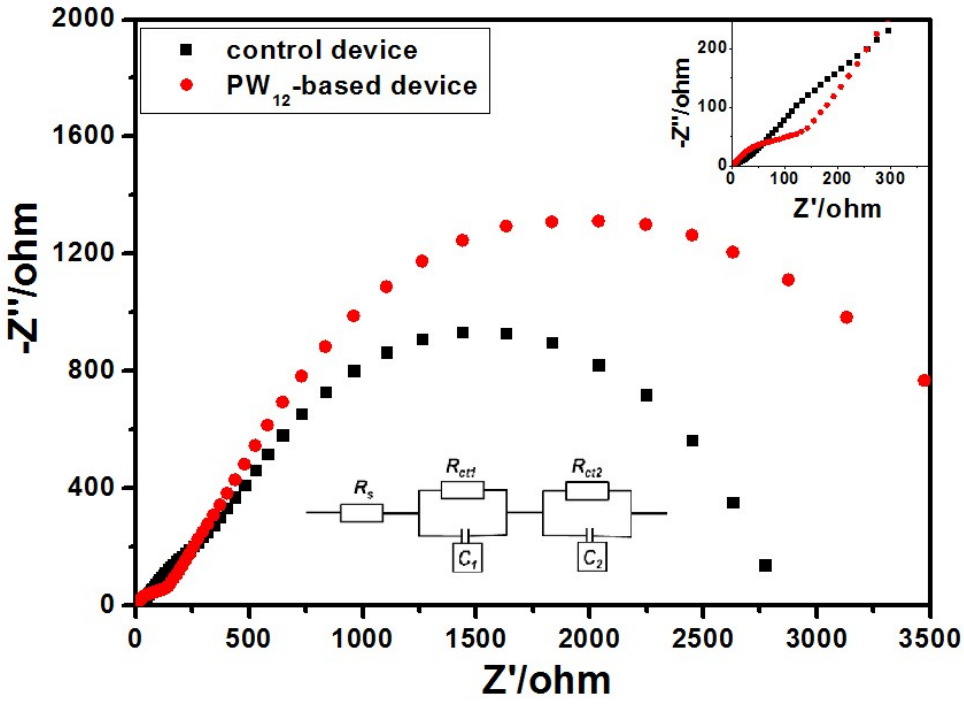

Figure S7. Nyquist plots of the devices with and without PW_{12} additive.

Electrochemical impedance spectroscopy (EIS) was carried out under dark condition at 0.1V in the frequency range from 0.1 to 100 kHz.

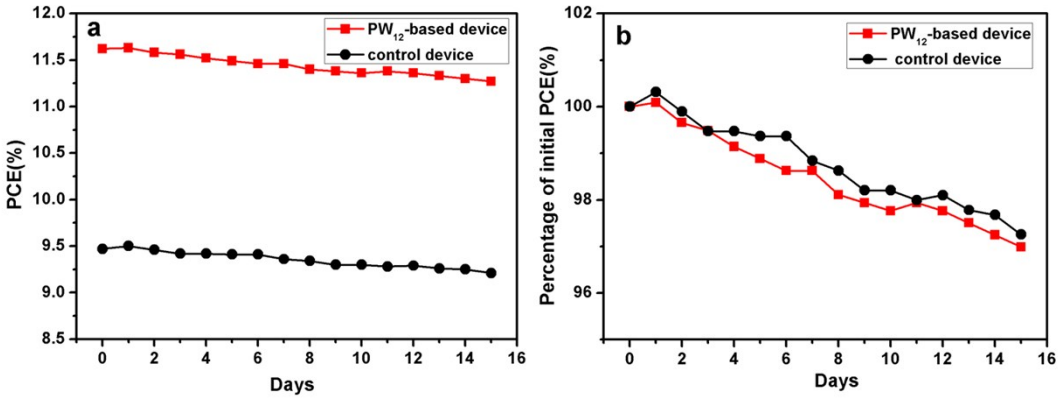

Figure S8. (a) Real PCEs as a function of time for PSCs with (15mg/ml) and without PW_{12}. (b) Normalized PCEs of PSCs as a function of time with and without PW_{12}. After each *J–V* measurement, the device was removed from light illumination and stored in the ambient air without encapsulation. The humidity of the atmosphere was ca. 30%.

The efficiency was periodically measured to check the long-term stability. The humidity of the atmosphere was ca. 30%. As shown in Figure S8, both the control device and PW_{12} doped device exhibited negligible degradation (<3%) upon exposure to air conditions after 15 days. In the device based on fully-printable technology, the 10-μm-thick carbon counter electrode can act as a water retaining layer, which also endows the device with excellent stability even without any encapsulation treatment. The control device retained 97.3% of its initial PCE after storage for 15 days. Similarly, PSCs doped with PW_{12} maintained 97.0% of its initial PCE value during the same aging period. Both the resulting devices exhibit promising long-term ambient stability, with negligible (<3%) loss in PCE. Therefore, although the large-grained perovskite film growth induced by POM should be dominantly responsible for the performance enhancement, the PW_{12} makes no distinct contributions to the improvement of the long-term stability.

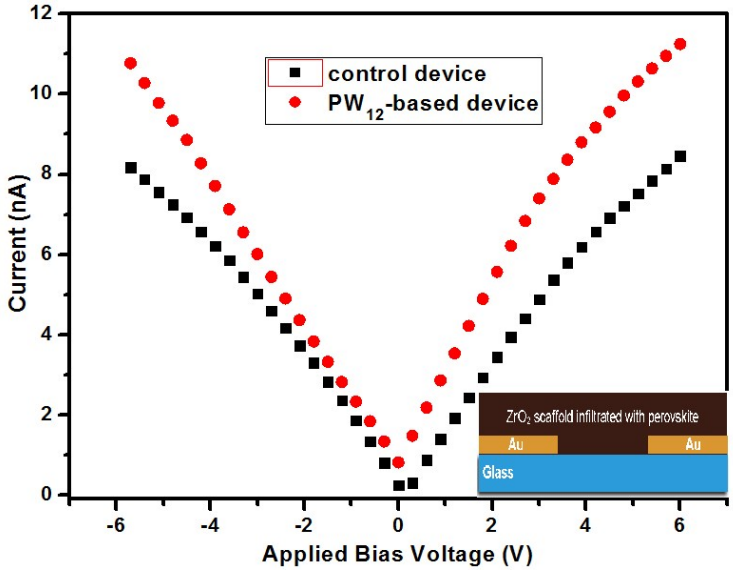

Figure S9. I – V characteristics of the in-plane hole-only device employing pristine and PW_{12} doped (15mg/ml) perovskite layers in dark. Inset: Schematic illustration of the device structure (Au/perovskite/Au).

To characterize the hole transport through perovskite within the mesoporous film in Han's fully printable architecture, the in-plane hole-only devices were fabricated by screen-printing mesoporous ZrO_2 scaffold layer onto the Au deposited substrate, constituting the hole-only device with the symmetric structure of Au/perovskite/Au.[5-6] The substrate was fabricated by deposition of a 150nm thick Au layer on glass with a channel width of 100μm via thermal vacuum evaporation, and then the channel were filled with the perovskite sample. Since the work function of Au is 5.1eV versus vacuum level, which is closed to the HOMO level of perovskite (5.43eV), the major charge carrier should be holes. The injected electrons are negligible and the device acts as unipolar device.[7-10]

The conductivities of the pristine and PW_{12} doped perovskite were evaluated by the equation (1), where L is the channel length (100μm), w is the channel width (1.4cm), t is the film thickness (150nm) and R is the film resistance calculated from the gradients of the curves.[8]

$$\sigma=L/Rwt \quad (1)$$

The obtained conductivity (σ) were 1.9×10^{-9} S·cm^{-1} and 1.35×10^{-9} S·cm^{-1} for PW_{12} doped perovskite and pristine perovskite infiltrated mesoporous ZrO_2 layers respectively. Based on the hole-only device, the conductivity of a material (σ) is equal to the product $ne\mu$, where n is the hole density, e is the charge of an hole and μ is the hole mobility.[10] The enhancement in conductivity observed from the PW_{12}-based hole-only device may be due to both the increased hole charge density and the enhanced hole mobility, suggesting that the large-grained perovskite film with higher crystallinity is indeed capable of reducing crystal grain defects and facilitating charge transport.

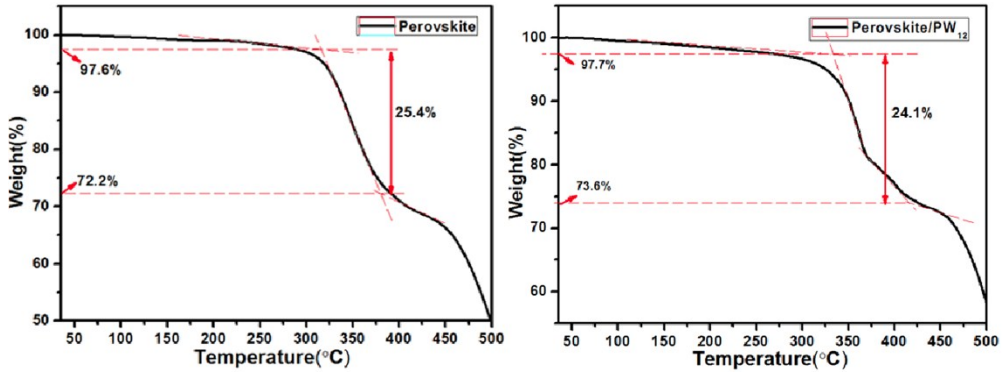

Figure S10. Thermogravimetric analysis (TGA) data of the pure $(5\text{-AVA})_x(MA)_{1-x}PbI_3$ perovskite and the PW_{12}-doped $(5\text{-AVA})_x(MA)_{1-x}PbI_3$ perovskite.

Figure S11. The films of both the pure perovskite and the PW_{12}-doped perovskite

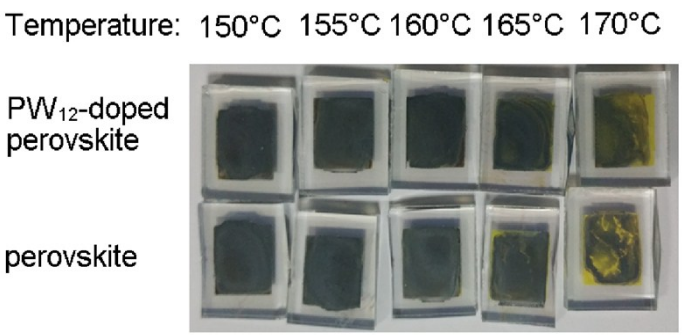

were heated at 165°C for 30min, the color changes (black to yellow) indicated that the perovskite (black color) degraded to PbI_2 (yellow color). The thermal decomposition temperature of both the pure and the PW_{12}-doped were *ca.* 165°C.

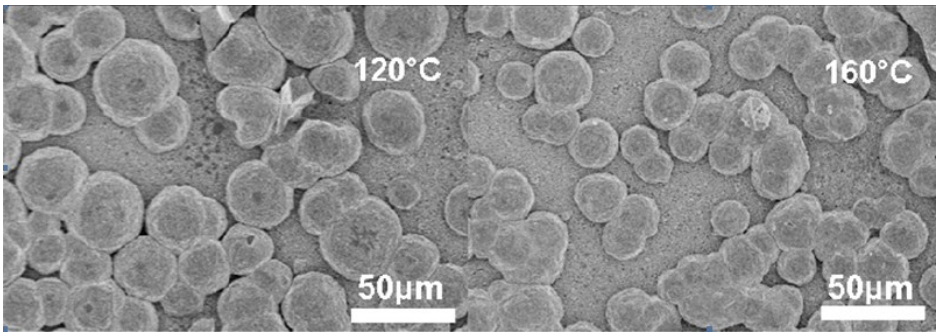

Figure S12. SEM photomicrograph of the morphology of the large grained perovskite films heated at 120°C and 160°C.

Table S1 Values for time-resolved PL characteristics by fitting the decay curves.

Precursor	τ_1 (ns)	f_1 (%)	τ_2 (ns)	f_2 (%)	Average τ (ns)
0mg/ml	1.75	58.60	23.74	41.4	10.86
10mg/ml	2.75	39.91	33.60	60.09	21.29
15mg/ml	1.46	18.98	34.48	81.02	28.22
20mg/ml	3.02	27.55	44.69	72.45	33.21

Table S2 Photovoltaic performance parameters of devices fabricated with different PW_{12} concentrations of precursors.

Precursor	J_{sc} (mA·cm^2)	V_{oc} (mV)	*FF*	PCE (%)
0mg/ml	18.00	807	0.63	9.17
10mg/ml	19.57	810	0.61	9.67
15mg/ml	22.57	801	0.62	11.35
20mg/ml	21.86	797	0.60	10.52

References

1. A. Y. Mei, et al., *Science*, 2014, **345**, 295–298.
2. H., Wu, *J. Biol. Chem.*, 1920, **43**, 189.
3. A. Abrusci, et al., *Nano Lett.*, 2013, **13**, 3124.
4. Y. G. Rong, et al., *J. Phys. Chem. Lett.* 2014, **5**, 2160.
5. Q. F. Dong, et al., *Science,* 2015, **347**, 6225.
6. Y. C. Liu, et al., *Adv. Mater.* 2015, **27**, 5176.
7. P.S. Rudati et al., *J. Appl, Res, Technol.*, 2015, **13**, 253.
8. H. J. Snaith, et al., *Appl. Phys. Lett.*, 2006, **89**, 262114.
9. S. D. Sung, et al., *Chem. Commun.,* 2014, **50**, 14161.
10. H. J. Snaith, et al., *Adv. Mater.,* 2007, **19**, 3643.